Heliyon 5 (2019) e02297

Contents lists available at ScienceDirect

Heliyon

journal homepage: www.heliyon.com

Fully automated tri-variational rebuilding of ideal solid-state models within mixed boundary conditions

Aykut Zongur *

State Ministry Office, Ankara, Turkey

ARTICLE INFO

Keywords:
Applied mathematics
Computer science
Mathematical analysis
Topology
Computer-assisted design
Computational modeling
3-Dimensional reconstruction
Morphology
Model-rebuilding

ABSTRACT

In this work, a rasterized mesh construction of our 3D solid-state model is generated to achieve an improved rasterization of a rigid-body surface using a series of polygonal model transfers. In the field of remodeling, auxiliary starters have been obtained from either ready-made or fabricated input point datasets. Building 3D solid meshes from clusters of inbound points to model objects is made possible by our method. Demonstrative illustrations of how the initial series of points can be transferred to mesh models by passing through the boundary conditions are presented using a customized method. A handmade weaving technique combines each different cluster of points, yielding a relevant transformation result. Additionally, newer remodeling methods involve more than the adaptation of boundary values to generate solid surfaces via finite restructuring of geometrical building blocks; our remodeling methods have been optimized in terms of both realism and computational costs. Our reconstructions are highly optimized to achieve high-quality and realistic results within a reasonable time. In higher-order creative restorations, our boundary conditions are regularized by quadratic equalizer functions. Areal-based regularizations are combined within mixed boundary values over 3D multigrids of finite differential combinations. Newly created solid models are reshaped by exclusive reconstructions to form our final models. Equally distributed multidimensional grids are seamlessly rebuilt via an ideal model-driven process with our tri-variational remodeling method that is constrained by a mixture of boundary conditions. Here, our remodeling method continuously triangulates the discrete topological structures as solid models. The final model shapes are triangulated as a consequence of postpolygonization by our unique reconstructors. An exact solution can be obtained via a convex hulling process on the preliminary finite fields by means of high-resolution configurations. Our 3D remodeling method using solid-state tessellation has opened the field to wider ranges of complete-gridding plans to achieve matchless enriched reformation capability, which makes our new solidification remeshing of models better than the majority of currently available methods.

1. Introduction

The transfer from 2D inbound point sets to 3D mesh models is made possible by the transition-construction method introduced in this article. Assembly models for this transfer have been established, which, compared to current methods, offer unique advantages that make the transfer possible [1]. After a quick start, the fields of cloud clusters are converted into polygonal mesh models with our 3D remodeling technique.

Immediately after passing to 3D model rebuilding, these data models can be distinguished in terms of how they store representations of newer models [2]. Point surfaces store the 2D rasterized graphical models [3]. Computerized design in multidimensions consists of regular volumetric grids that have all been resampled on finite space fields [4]. It is the highest resolution that originates from the frames of 2D multigrids, regardless of their density. In the case of high density, the density is examined, which is why the spatial resolution is one of the decisive factors for minimum system requirements. The necessity for peripheral surroundings results in a colorless normal orientation [5]. High-density standard shape molds were selected for solid molding; therefore, higher-density models will be obtained when using all the 3D data in order to take advantage of them in advance.

Our selective system adjusts well in a high-quality parcelization method starting from the initialization of initial value problems in which the location is different from the originally estimated mapping location [6]. As verification of our method could have been achieved with normal

* Corresponding author.
E-mail address: z_aykut@yahoo.com.

https://doi.org/10.1016/j.heliyon.2019.e02297
Received 18 July 2019; Received in revised form 9 August 2019; Accepted 9 August 2019

estimates of feature settings, the overlay liners are directly initialized from the unstructured initial values [7]. The system automatically completes the next pass to process the initial values, which have been obtained in the boundary condition process. Postprocessing of boundary values is explicitly used in all finite triangular elements to realize mesh remodeling. To align the surfaces, the functioning processes can be reiterated to the last recursions set for the direct 3D seaming of all finite triangles. An iterative and recursive flooring style is specifically designed for specially predetermined staging values, which outnumber the convergence thresholds of others.

For our latest projection, a cluster of clouds is the collection of an unconnected 3D pointset. The underlying reason for use of the term "clouds" is that they have the appearance of interstellar planets in a galaxy space system when the unconnected points are visually clustered. These interclouds pass as in-line model carriers to provide locational information values alone. Wherever point-cloud clusterings utilize normal direction estimations, they are then available for use as relocation indexes. Although the reformed point collections can be classified as a world-class model, it would be advantageous to start with them in lieu of the actuators [8]. Our remodeling method drives the concepts of model shaping to that point before the start of reconstruction of even realistic future surface areas. The model datasets in this work (see Fig. 1) are referred to as base models and are used as reference models in a wide range of reshaping for our conclusive evaluations.

2. Related work

2.1. Alpha shapes

The first technique is alpha shaping [9]. Alpha shapes are generalized convex hulls that are calibrated by an α-parameter to point clouds, which are alpha complexes of all shapes in the context of a solid, as defined in Eqs. (1) and (2).

$$p \in B.C._{\alpha} \Leftrightarrow B_p \cap C.H._{\alpha} \neq \varnothing \tag{1}$$

$$p \in C.H._{\alpha} \Leftrightarrow B_p \subseteq B.C._{\alpha} \tag{2}$$

Here, p is the current point in a general shape, C.H. is the convex α-Hull of the α-diagram, B.C. is the boundary conditions over all borders, and B_p is an α-Ball on the α-diagram of the target shape. When $\alpha \to \infty$, the alpha shape becomes a convex hull over P, but in the case of $\alpha \to 0$, the alpha shape becomes P itself. Polygonal shapes are reformed from the prespecified Delaunay polygonization for other values of alpha. The alpha shapes are reshaped by incrementally lifting off the affected sides where $|x_i - x_j| < \alpha$, where $i \neq j$. As soon as one of the border edges or faces is removed, the faces or frontiers are eliminated from the alpha complex upon building the new alpha shapes with respect to the selection of encirclement radius in Eq. (3).

$$r_p = \frac{|p_i p_j| \cdot |p_j p_k| \cdot |p_k p_i|}{4 \cdot |p_i p_j p_k|} \tag{3}$$

where r_p is the smallest circumsphere radius of B_p. Particularly in regard to creating real-world objects, alpha shapes are not usually useful in the formation of new surfaces. Only one α-value is determined with the intention of using a wider representation power of the entire surface since the α-parameter is globally chosen. This choice becomes irresistible and irreversible, especially when the sampling form in P is nonhomogeneous. Alpha shapes do not have to be manifold, and alpha complex generation is random.

2.2. Voronoi hulling

The Voronoi hulling technique recomputes the triangulated form of any given point set surface despite having no prior information on the normals of the vertices. This previously established method eliminates the triangles by only considering the nodes of the next-generation Voronoi diagram [10]. After brief reformation of the Voronoi hulls, the method chooses all Voronoi vertices from the remotest opposite side of each pair of sample points [11]. Next, it will find the triangulated surfaces for the first-order Delaunay model and the selection of most appropriate Voronoi vertexes. The only triangles that are kept are the elements of three vertices for the sampled points, as in Eq. (4).

$$V(\boldsymbol{p}_i) = \left\{x \in \mathbb{R}^d : ||x - p_i|| \leq \left||x - p_j\right||, \forall j \neq i\right\} \tag{4}$$

where $\boldsymbol{p}$ is some set of points on the site area and x is any point on the polygon elements that aligns with the Voronoi regions called $V(\mathbf{p}_i)$.

2.3. Signed distance function

One of the long-established distance function approaches is linked with distances, resulting in global interpolation of surface-organization problems [12]. Since this approach redefines and updates the function F to some extent, F will make a new approximation of a surface at the assigned distance. When the goal is to reinterpret the definition of the final function, a few new constraints are set on each sample point of F as a zero-set of the distance function. Additional constraints are added for the zero condition of the baseline solution. “Off-Bounds” and “Out-Bounds” points were pinned and redefined, as these impose constraints on F such as being equal to positive or negative values. Whenever the surface manifold self-folds inward on itself, area markings are taken within the boundary line ranges where all interior and exterior constraints conflict with each other. The conflicting faces are found in these free-formed splines. The on/off-surface elements are determined using Eqs. (5) and (6).

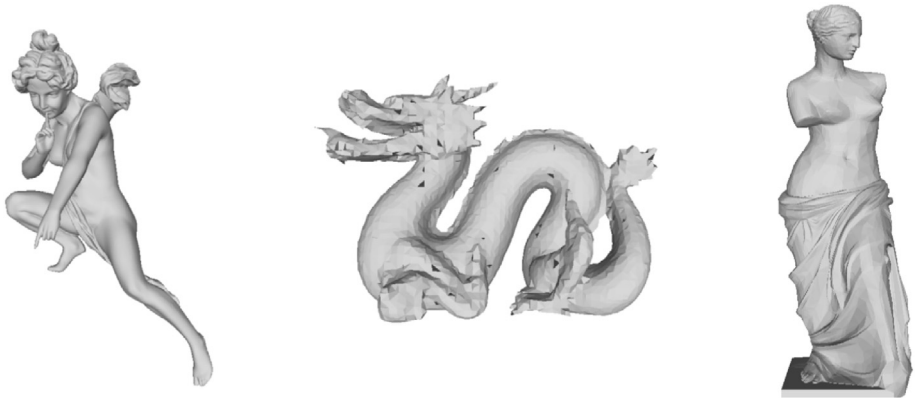

Fig. 1. Shapes from historical sites.

$$s(x_i) = f_i = f(x_i, y_i, z_i) = 0,\ i = 1,\ \ldots,\ n.(\mathrm{On} - \mathrm{the} - \mathrm{Surface}) \tag{5}$$

$$s(x_i) = f_i = f(x_i, y_i, z_i) = \pm\, d_i \neq 0,\ i = n+1,\ \ldots,\ N.(\mathrm{Off} - \mathrm{the} - \mathrm{Surface}) \tag{6}$$

The signed distance function solution is chosen to solve *F*, which was very well represented with all of its integral components for a weighted total sum of basic functions where constraint-centers, parameterized weights and global support functions are found. A set of weight parameters could only be found for each value by curve fitting. The presence of constraint parameters yields Eq. (8) from Eq. (7).

The kernel function has an extended global support presence, so the linear least-squares estimations that seek the parametric weights form a relatively poorly conditioned condensed pattern with a wholeness approach. The results prove that this will become difficult to robustly solve when the size of the linear system increases. When special-purpose kernel basis functions are used to remake surfaces from unlimited point sets, dozens of improvements will be required by F.

$$\phi(x - x_i) = x - x_i \tag{7}$$

Multilateral techniques are obtained for rapid appraisals of the final functions. There are preliminary functions that reduce the number of required constraints to be appraised at one particular point where the centroid of shapes is remote with only one constraint. These events are used during the approximations in the following equation:

$$s(x) = p(x) + \sum_{i=1}^{N} \lambda_i \phi(|x - x_i|) \tag{8}$$

Branch and bound design modeling can also be used to further redesign the surface area in this respect. Regions are bounded according to a certain intended adaptation by iteratively fitting fewer constraints on any given input data point set.

2.4. Fast fourier transform

Our method works with FFT by deploying implicit functions for delimitation and takes CFT as the basis [13]. The method was reinforced by numerous chains of algorithms since it has an FFT-driven technique as its origin. Mainstream works involve a calibrator function implemented according to Naiver-Stokes theory [14]. This function expresses the volume of the target surface area by integration of a finite field estimated from any directed point sets. Calibrations provide coefficients for the post-Fourier transformations that serve as smooth integrators for surfaces and were previously integrated from samples of oriented point clouds. The final result of a calibrator can be achieved by recomputing the Fourier coefficients and rolling them back to discrete Fourier transformation from that point on. The most recently obtained surface elements are then reshaped with the help of a 3D surface creator algorithm called marching cubes. The full complexity of all surfaces on any arbitrary input point cloud is maintained with the assistance of hull configurators as globally supported kernel adjustment functions over each vector field. Because of their globality, FFT-driven methods are robust to shape formations and resistant to many types of deformation by means of both sample orientations and locations of nonuniform resampling from inbound point datasets. Deficit input data-origin problems are smoothly dependent on the formalities of the smoothing outcome. However, this technique still has major drawbacks, such as spatial-area management and the lack of control of temporal coherence. Allotment of an *nxn* regular grid also superimposes impractical issues of using such an approach. In particular, creation of high-resolution shapes is sought while renewing the content.

Very well-designed future methods are mostly used for refinement through adaptation. These approaches will probably take portions of sizeable models via dimension-adaptive partitioning and the divide-and-conquer approach on the basis of numerous locally fitting FFTs, which are blended into one independent calibrator function. Previously nonexistent blending capability is an indication of how these approaches are combined for use in MPU with the sole intention of making blenders for the inferior subspace curves. While this approach appears to have a large degree of qualifying scalability relative to the existing models from the start of initialization, local area meshes used to blend local FFT constructions could also make this method less resilient. Eqs. (9), (10), (11), and (12) summarize the working principles.

$$\widehat{\chi}_M(l, m, n) = \int_M \nabla \cdot \overrightarrow{F}(p)\mathrm{d}p = \int_{\partial M} \overrightarrow{F}(p), \overrightarrow{n}(p)\mathrm{d}p \tag{9}$$

$$\widehat{\chi}_M(l,\ m,\ n) = \int_{R^3} \chi_M(x,\ y,\ z) e^{-i(lx+my+nz)}\mathrm{d}x\mathrm{d}y\mathrm{d}z \tag{10}$$

$$\widehat{\chi}_M(l,\ m,\ n) = \int_M \nabla \cdot \overrightarrow{F}(p)\mathrm{d}p \approx \frac{|M|}{N} \sum_{i=1}^{N} \langle \overrightarrow{F}(\overrightarrow{p}_i), \overrightarrow{n}_i \rangle = \frac{1}{N} \sum_{j=1}^{N} \langle \overrightarrow{F}_{l,m,n}(\overrightarrow{p}_j), \overrightarrow{n}_j \rangle \tag{11}$$

$$\overrightarrow{F}(l, m, n) = \frac{i(l, m, n)}{\left(l^2 + m^2 + n^2\right)} \tag{12}$$

where $\widehat{\chi}_M$ is the characteristic function for a solid model of *M*, $\overrightarrow{l} = (l, m, n)$ are the Fourier coefficients of a characteristic function, and $\overrightarrow{n}(p)$ is the unit surface normal at point p.

2.5. Wavelet

One last approximation, called the wavelet approach, is also very similar to the previously described FFT method, also using a calibrator function to obtain new grids with oriented cloud points through a special form of Stokes theory [15]. In contrast to the continuous time Fourier transform, this method can register only the orthogonalized forms of wavelets [16]. The Fourier sample basis was determined from all available Fourier coefficients. This requires calculations of all overlapped disjointed point samples. These wavelet-formed basis samples are built on support function models. Unlike the Fourier basis functions, the wavelet counterparts are obtained by computation of every wavelet function coefficient for the compact superimposed samples. Eqs. (13) and (14) are progressively building process support functions that are finalized in Eq. (15).

$$c^e_{j,k} = \int_{R^3} \chi_M(x) \psi^e_{j,k}(x)\mathrm{d}x \tag{13}$$

$$c^e_{j,k} = 2^{3j/2} \int_M \psi^{e_1}\left(2^j x_1 - k_1\right)\psi^{e_2}\left(2^j x_2 - k_2\right)\psi^{e_3}\left(2^j x_3 - k_3\right)\mathrm{d}x \tag{14}$$

This approach has various practical advantages over FFT-based approaches. This was ultimately considered a more effective approach with lower spatial-discretization complexity by the packed form of two or more interlaces, which are stored as the wavelet coefficients for sample points.

$$c^e_{j,k} \approx 2^{\frac{3j}{2}} \sum_i \overrightarrow{F}^e_{j,k}(p_i) \cdot \overrightarrow{n}_i d\sigma_i \tag{15}$$

where ψ is a univariate wavelet function with compact support and *c* represents the discretized coefficients.

3. Methodology

Assembly in general starts by remeshing the original cloud points using areal base rasterization in our design models. Similarly, there exists

an operational groundwork for the raster surfaces of free-body remodeling, which must retain the key properties described here. Regridding then results in the most ideal plot settlements for the greater surface areas. Contrary to the fact that the less-curved areas are tessellated with fewer vertices, our high-class, finer-granularity areas absolutely reflect numerous nodes for parceling out the unparcelled zones. In addition, valuing out the interpolants amid vertexes of partially cloudy data models is continually executed to redefine our work; nonetheless, this process would work without ancillary augmentation.

Our general method generates restructured meshes while benefiting from the feature manipulations of surfaces utilized in previous methods. Premier mesh refiners are utilized for definitive geometrical texturing. Additionally, our decisive functional reconstructors continuously display the discrete models by enabling self-interconnections among the node vertices. These unique piecewise continuous function spaces make high-definition plots possible with an interstellar-like distribution since nothing would be associated with clustering otherwise.

One 3D location plus one set of color information (both in the context of RGB and textural terms) and all additional normals are involved in one common, the connected analytical framework. The layer surfaces are used to represent each other in different node points with one-to-one and onto mapping. Unless the system has been highly calibrated, the normal directions must also be estimated. Connection sets indicate which of the alternatives are collocated to generate the surface topology [17]. Well-arranged geometries are subject to collateral mesh-based regularization of triangulation, which is achieved by our restructuring elements for the surfaces.

The topological conditions of our finite-sized interconnected mesh elements are satisfied in a tri-state independent plan with one two-common edge that could have its own calibrator over any surface of interest. Topology preferences are those that have one two-sided triangular element with common edges by later-reformed triangular blocks compared to our advanced area maps. The united combination of each element with others is tessellated by our method that combines all elements into one overall mesh model.

3.1. Design

Not every directed normal for 3D layers is manually gauged with a single point set in which all of the orientations are manually redefined in new locations. Either manually or by utilizing the tri-dimensional points in the cloud, our methodology can determine the normal directions of surface clouds by our locating operations that are fully compatible and constructed with all types of constructors. Nonlinear fitting of each cloud point to the nearest subnet graphs is performed by any operating fetch routine for a specific layer. Local surface normals are locally floored over planar tangents. Our newly established method determines the closest neighbors of each element in each location by batch processing while being adapted to finite fields. Since our method makes use of adjacency neighborhoods independent of distance, new models can be formed using maximum details in compact locations, including many more polygons for a given surface. Another role is to estimate the sparser sites of coarsely distributed point clusters. Layer hulling first computes the normal-oriented surface models.

Surface plane-lines are equal to the local normals in this work. Our model designs are indeed practically designed, unique techniques to model building structures. The collections listed here facilitate highly versatile directional normal estimates from the highly complex regions using our uniquely defined functions during systematization. How the normals will be deployed is also reformulated below in Eq. (16):

$$\iiint_{\partial\Omega} \eta \nabla u_n \cdot \nabla v \cdot \boldsymbol{n} \, \mathrm{d}x \, \mathrm{d}y \, \mathrm{d}z = \iint_{\Gamma_N} \eta \nabla u \cdot \nabla v \, \mathrm{d}x \, \mathrm{d}y + \iint_{\Gamma_D} fv \, \mathrm{d}x \, \mathrm{d}z, \ \forall v \, \varepsilon \, V_n \tag{16}$$

where n is the normal estimate.

As our problem sets were initiated from the first initial value conditions, our latest resolutions have refined all n-perspective view models for which the shape models are to be generated via our remodeling method. The approximations are automatically applied with a customized 3D solid-state model from which any polygonal surface is directly rebuilt. Our method was used for full remodeling while the structures of interest were under construction.

Newly created surfaces are formed by multiphase blending of our surfaces. Our structural synthesis method considers the construction essentials for any shape area model that is remodeled using our finite building blocks. High-dimensional remodeling is achieved by our newer reconstruction architecture.

Model areas of the restructured facade coating are reshaped upon application of our shape design. The final solid models are covered for the reconfiguration of our mesh-regulation events. The varying-dimensional grids are reinstated by means of nonlinear multi-tessellation. After our convex hulling was fully automated with custom specifications, recent 3D model designs were templated in terms of our dimensionality-controlled shape designs.

3.2. Model

The triangulated meshes together with the whole-surface normals aligned with the clustered points can be transferred to finite-state models with respect to our working outflow. A proprietary finite-state resolution technique was duly planned, similar to our in-house design specialty, that triangulates the overall quadrilateral meshes with normal orientations across the entire outer facade. The difficulty with this method is determining the vertexes that will be linked or might not be directionally oriented without another option. The density may vary; thus, far lower resolutions with intervertical distances among the vertices may be a well-established option to achieve total volumetric model assembly. Proximal neighborhood collections are subjected to exclusive solidifiers of the object models to achieve an overall regular layout order, as given by the equations.

Here, the three-dimensional oriented features make the results slightly more precise in terms of surface orientation. Rediscovered calibrations for an interelement polygonization with multicriterion eliminations are rapidly calibrating the clusters; however, these criteria are not the only variables that do not comply with the rest. Extra factors are the variants of our rebuilding directives. More attention was paid to distinctively combining the finite field rebuilders. Special measures can be used to define subsequent elements for which a new interlocking junction of surface points can be formed. The triple form of the reformulation is rewritten as in Eq. (17).

$$\sum_{i=1}^{n}\sum_{j=1}^{n}\sum_{k=1}^{n}\left(\int_{\Omega}\eta\nabla v_{\mathrm{i}} \cdot \nabla v_{\mathrm{j}} \cdot \nabla v_{\mathrm{k}} \, \mathrm{d}x\mathrm{d}y\mathrm{d}z\right)c_i c_j c_k = \int_{\Omega} f v_i \mathrm{d}x + \int_{\Gamma_N} h v_j \mathrm{d}y + \int_{\Gamma_D} g v_k \mathrm{d}z. \tag{17}$$

where c represents complementary coefficients of the n-vector field components.

All of our aligned nonlinear difference equations at zero conditions are encompassed by the tangential nonlinear lines within a mixture of boundary conditions on which the boundary values were applied to the frontiers. Manual conditioning of the frontiers will consequently result in an extra factor for the total consolidation of solid objects. When multi-state finite differential systems are to be reconditioned with our final operating conditioners over the quadratic areas, Eqs. (18), (19), (20), (21), and (22) can be used, and they are regulated with a mixture of B.C. in Eqs. (23) and (24):

$$K \cdot \overrightarrow{V} = F, \ over \ the \ \overrightarrow{V} = \langle v_1, \ v_2, \ \ldots, \ v_n \rangle \tag{18}$$

$$K_{ijk} = \int_{\Omega} \eta \, \nabla v_i \cdot \nabla v_j \cdot \nabla v_k \, \mathrm{d}x \, \mathrm{d}y \, \mathrm{d}z \tag{19}$$

$$F_i = \int_{\Omega} f v_i \, \mathrm{d}x \tag{20}$$

$$F_j = \int_{\Omega} f v_j \, \mathrm{d}y \tag{21}$$

$$F_k = \int_{\Omega} f v_k \, \mathrm{d}z \tag{22}$$

subject to

$$v = g \quad \text{on } \Gamma_D \tag{23}$$

$$\eta \frac{\partial v}{\partial n} = h, \ (\eta \nabla v).n = h \quad \text{on } \Gamma_N \tag{24}$$

where $\boldsymbol{n}$ is the vector of the surface orientations for the normal directions corresponding to that area. g is the Dirichlet boundary values on Γ_D Dirichlet boundary conditions, and h is the Neumann boundary values on Γ_N boundary conditions, which form the mixed boundary conditions together.

Multiresolution tasking along with the normal computing has transformed partially differentiated discontinuous meshes into fully ordered continuous meshes that are attained on the basis of each volumetrized element. The volumetric meshes were once valued thoroughly.

The generation of solid-state models was achieved with our unique polygonization techniques that centrally rely on an exhaustive design of equilateral mesh elements. Here, our methods for interwinding state changes are the key to these specially written mesh procedures. Illustrative examples of our solid models that are continuously optimized have also been discussed. The triangulations and quadrangulations have been customized. Alternative redesigns proposes offer a unique combination of advancing finite time/space variations that are interlinked with either triangulation or quadrangulation. All of these phase changes were performed via a new polygonization method, which involves the time and space-discretization over the dimensions of the X, Y, and Z axes in this work. Solid gridding on clustered regions is a driving force for the transfer of all discretized state models. Furthermore, our model involves processing the tri-variational state transfers for remeshing the interelement meshes through our finalized 3D surface grids. Multiple illustrations have been provided of our solidification work that has adapted the reconstructive restorations of systems in the form of solid shapes. Collocation of faces is achieved as in Eq. (25):

$$K_{ijk} = \frac{e_i \cdot e_j \cdot e_k}{8|T|^2} \int_T \eta \, \mathrm{d}x \, \mathrm{d}y \, \mathrm{d}z \tag{25}$$

The η coefficient does not have to be constant, as this is delimitated from intervals such as $[\alpha, \beta]$ that might have to take measures for any values in functions where

$$0 < \alpha \leq \eta(x, \ y, \ z) \leq \beta \quad \forall (x, \ y, \ z) \in \Omega.$$

The final set of initial values is elliptically conditioned in a well-designed method that results in another level of feature settings over all boundaries. Our complete mesh-generation system involving functional modeling is an outstanding advancement for the delimitations of boundary conditions. Solid objects were completely mapped one-to-one to become complete models with our skinning approach. Moreover, 3D shape modeling was incorporated to achieve a full polygonal grid of the reshaped models. How that rigging addresses automated refinement will be realized with our remodeling plans. In the interim, this method can be used as an accurate structural synthesizer as the foundational principles of our solid-state models for which any noise-eliminating spatial axis models are established. Our remodeling method solidifies the cross-border delimitations that had become out of bounds. Cooperative volumetrization is incorporated into our blended state of mixed boundary conditions alongside the boundary edges. Improper formations of boundary conditions are regulated within our limits of convergence where the boundary lines are established. The rearrangements for collocated faces are tri-laterally defined as in Eqs. (26), (27), and (28).

$$e_i = \frac{L}{8} \int_{-1}^{1} h(1-\lambda)\big((1-\lambda)v_j + (1+\lambda)v_k\big)\mathrm{d}\lambda \tag{26}$$

$$e_j = \frac{L}{8} \int_{-1}^{1} h(1+\lambda)((1-\lambda)v_i + (1+\lambda)v_k) \, \mathrm{d}\lambda \tag{27}$$

$$e_k = \frac{L}{8} \int_{-1}^{1} h(1-\lambda)\big((1+\lambda)v_i + (1-\lambda)v_j\big)\mathrm{d}\lambda \tag{28}$$

where $L = \| \, v_{k,k,i} \text{-} v_{j,i,j} \, \|$ is the actual length of the triangle edges for unit elements and the independent variable λ for our unit triangles is bounded to the closed interval -1 $\leq \lambda \leq$ 1.

4. Experimental

Having discretized the area parcels for any given initial conditions of model shapes, our solid-state model design was extensively tested in practice. After considering all equi-edged polygonal mesh faces beyond the boundaries, discrete computational structures of clusters of points for our solid-state model were distinctly continued with spatial 3D continuation techniques that rendered it by weaving the midpoint values of interconnected meshes across the entire surface. Here, the adaptation process of fitting solid planes is remeshed in solidified model forms and postprocessed in an adaptive way.

Our models are no more imperfect than those that have already been defined; faults due to textured mapping of the borders along front-lines result in more irregularity in the edges. Our unique models regularize the irregular mesh elements by converting them into regular meshes. An underlying cause of faulty boundary conditions is the edge irregularities around surfaces that are curbed by fault-free actions and the boundary-arranging properties that are applied by default [17].

Wire structure models have been remeshed over time. The ultimate extirpation of whole tri-directional approximations is reduced to feature extractions obtained from our newly regulated finite element space. Regardless of how frequently these reshapings are observed in exact approximations, new shape models are usually remade via estimates of nonparametric parametrization.

The corners of the designed shapes are convolved by providing moldability to the types of solids they have been assembled from—either sphere or cylinder; this generally results in shape invariance. The final product of our remodeling method is an executable mixed mesh that has to be sequenced with an arrangement of 3D tiles. As illustrated in Fig. 2, the final recreations are resampled, similar to the method used for our model reconfigurations.

The final simulation results were obtained by an x64 Intel(R) Xeon 2.0 clock cycle GHz processing unit on a computer workstation with nearly 16 GB of RAM equipped. The final results were emulated in our simulation run time, where the machinery has a 4 GB video card for providing high-end weavings of disjoint structures. The computational models that were simulated were lost in the flurry of these scenarios. Our overall approach is more likely to evolve into a functional design for unshared source allocations in our future work. The ultimate state of our system would prove effective for use in emulations at the higher-quality end of the performance tests.

The tri-form layout used to reconstruct images was enriched through

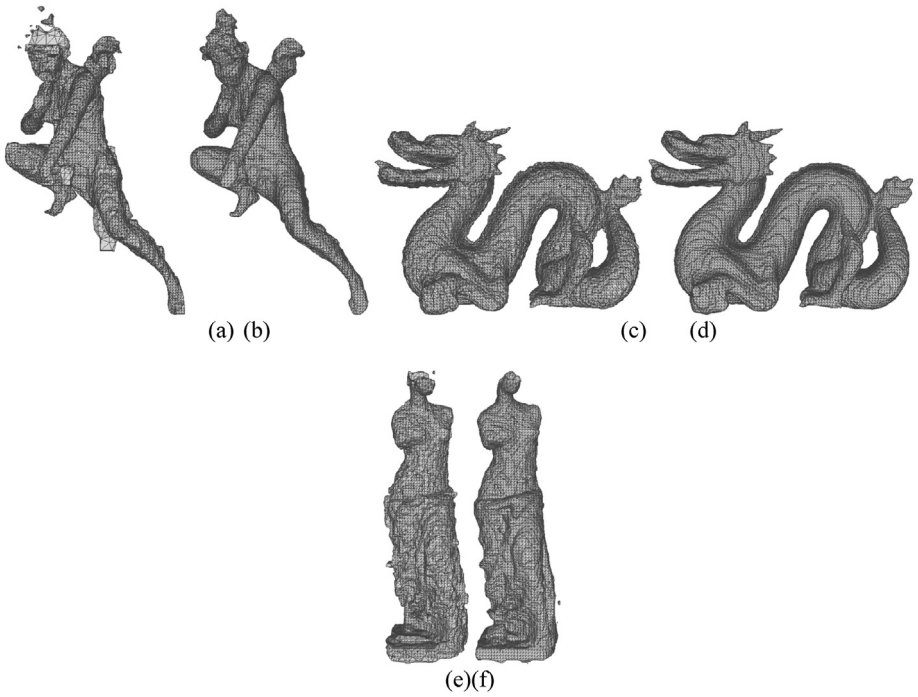

Fig. 2. Solid creations rebuilt for the 3D manufacturing of recreation areas with wavelet approximations (a–f).

our surface lining. Having been enriched by the rigging of polygonal meshes, the newer remodeling method was applied for triangulating the free zone elements via our reconstructive enrichment processing. Triangular meshes were reconstructed via 3D shape building. Elliptical difference equations have been installed onto the point sets of surfaces. Our unique Poisson reconstruction model eliminated the disoriented points from the surface with higher-caliber construction operations relative to other previously used approaches for general system optimization. The areas of surfaces are remodeled as a final result of our modeling processes. Our mesh-based polygonization design used a unique method with a quantitative approach that has been reconditioned and renewed as shown in Tables 1, 2, and 3.

If more powerful machinery-powered computers are used, the performance of our method will exceed that of previously used specimen models. Prior to testing the implementation, a forward-looking view was used that accomplishes comparative appraisals in an alternating fashion.

The resamplings reported herein as example models with varying levels of impermeability match well with our results. The numerical results in the volume-time-quality tri-state resolutions increase nearly exponentially. Even though the compactness increases, the runtimes of the models tend to be optimal. The time, volume and manufacturing performances of our proposed techniques were compared to the work-performance charts of other techniques at each level of performance/

Table 1
Building times, maximum volume allocation, and number of layer elements in the rigging of the angel sample recreated by different remodeling methods.

Methods	Time (sec)	Spatial Reservation (MB)	# of Elements
Alpha Shaping	11.705	55.3	3,076,614
Voronoi Hulling	62.915	46.6	**3,323,067**
Smooth Signed Distance	45	7.46	411,824
Haar Wavelet	**0.733**	**1.69**	25,766
Wavelet D4	2.29	1.76	26,920
FFT	1.582	1.91	62,164
Our Constructor Model (Postprocessing)	27.75	22.8	1,261,588

Bold indicates utilization index.

Table 2
Building-times, maximum volume allocation, and number of layer elements in the rigging of the dragon sample recreated by different layering methods.

Methods	Time (sec)	Spatial Reservation (MB)	# of Elements
Alpha Shaping	2	0.38	20,517
Voronoi Hulling	0.87	0.33	16,228
Smooth Signed Distance	4	**0.287**	15,458
Haar Wavelet	**0.167**	4.35	57,834
Wavelet D4	0.614	4.16	55,292
FFT	1.616	9.28	**260,388**
Our Constructor Model (Postprocessing)	1.1	0.7	22,880

Bold indicates utilization index.

Table 3
Building-times, maximum volume allocation, the number of layer elements in the rigging of the Venus sample recreated by different layering methods.

Methods of Solid Works	Time (sec)	Spatial Reservation (MB)	# of Elements
Alpha Shaping	1.44	1.15	56,219
Voronoi Hulling	8.889	3.76	**267,366**
Smooth Signed Distance	10	1.01	56,226
Haar Wavelet	**0.167**	1.67	26,084
Wavelet D4	0.549	1.65	25,626
FFT	1.500	**0.15**	5,232
Our Constructor Model (Postprocessing)	3	2.58	142,492

Bold indicates utilization index.

cost. Our study suggests a way to make configurations scalable to the highest resolutions and promises to be effective in completing these studies due to successful tri-variationality.

The mesh results have been found as the definite editions of our alternatingly varying geometrical shape building blocks with the inclusion of a variety of axial reconstructors that have all been built in as our readjusted special work. The method is redesigned to generate the best examples of our unique, locally enhanced global-scale alignments for remodeling. Reconstruction of our model-state buildings is demonstrated

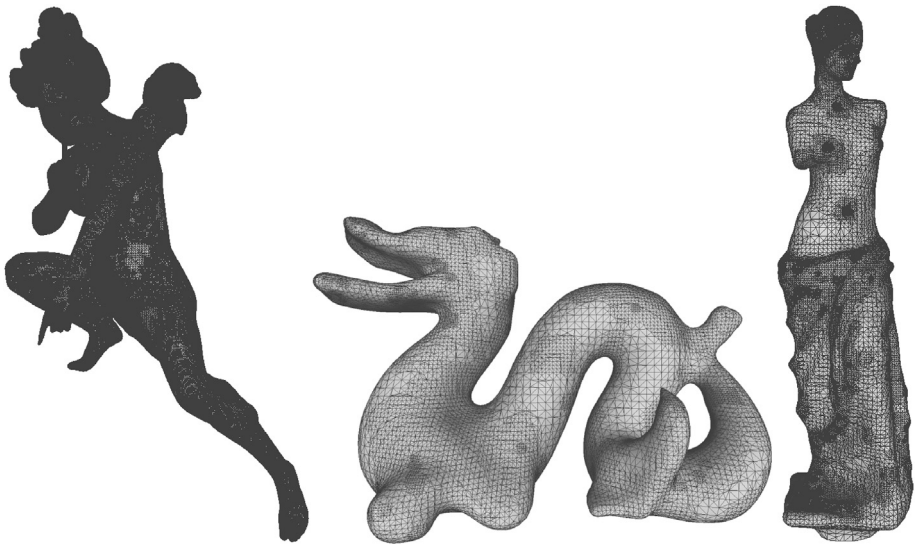

Fig. 3. Recreated solid-state models have been attained in various ways with shape-invariant options.

in an unprecedented way, as shown in Fig. 3.

Not all solvers usually automatically adapt the resolution for partial equational differentials on open fields. Our patchworks continuously interconnect the piecewise polynomial subspaces with crosses over each finite element. Approximated function coefficients are reconfigured to obtain the most ideal solutions. It is the fine granularity of our triangular polygons that accurately gradates the precision of solution approximations.

This work uses our remodeling method to process the relocations of overlays that have been processed via clustered clouds within the convergence limits for the upper/lower bounds of the solid shapes. Alignment-related changes are made for the surroundings of all shape models that have been regulated over our overlays. Formal spatial fault analyses of triangular areas are synthesized as shown in Table 3.

The reference models have been used for sampling bases that are aimed to be surpassed by ours from the 2000s onwards [18] and then have been regularly modified until unique rectifications are created on a one-to-one basis. Here, our enhanced tessellation method for remodeling has resulted in highly developed results compared to those reported in previous works. In fact, our method is superior to the others and unique in that it enables transference of model values in either direction. Where the fully automated area conditioners crossover, the results are much better than those that have been adapted to exterior factors such as reflexivity, shading, and lighting. Watertight serial mesh orderings were indispensable after processing cuts were used. Ordered areal meshes are tiled in a way that might meet the highest building standards for completeness. Here, our enriched method is applied quite effectively.

The errors in varying norms listed in Tables 4, 5, and 6 were computed with our autorefinement finite triangulator that corresponds to the nearly exact solution offered by the approximations over a specific problem range.

5. Conclusion

Advancements have been elaborated in this cascading style of rebuilding phases due to our proprietary properties for highly advanced realistic models. Here, the solid model outlines achieved optimal representation of the original object, even when no other option was available with which to achieve fine granularity, which varied. Additionally, such granularity renewal for overlaying is weaved by our wireframe solid surface overlay. Moreover, high-capacity zone parceling is maintained through a minimum trade-off between computational costs and resolution along the highest possible dimensionalities. The boundary conditions where all models have been reworked over the frontlines were to be blended with our new boundary conditions in versatile remodeling. Our works have already eliminated the dependency on direct 3D nonlinear least square fittings. The advancing execution modes of refinements were customized with definite shape-adaptable modeling methods that are unique to our work. The rearranged model shapes were adapted in a self-adaptive manner for executing our unique solid-state model. Our automatic model refinements took advantage of auto-

Table 4
A posteriori errors occur with the finite triangular space-discretization over a corresponding Angel-problem domain that is analyzed with our solution approximations in the assorted norm manifolds for each maximum lowest angle.

Angle	# of Elements	$\|\| u_{ideal} - u_h \|\|_L^2$	$\|\| u_{ideal} - u_h \|\|_E$	$\|\| u_{ideal} - u_h \|\|_{L\infty}$
$\pi/12$	315,396	0.275848858	0.523896422	0.116563984
$\pi/10$	378,474	0.029374072	0.078004798	0.011838717
$\pi/8$	473,094	0.028873369	0.013075942	0.001206186
$\pi/6$	630,794	0.022939922	0.002222683	0.000123495
$\pi/3$	1,261,588	0	0	0

Table 5
A posteriori errors occur with the finite triangular space-discretization over a corresponding dragon-problem domain that is analyzed with our solution approximations in the assorted norm manifolds for each maximum lowest angle.

Angle	# of Elements	$\|\| u_{ideal} - u_h \|\|_L^2$	$\|\| u_{ideal} - u_h \|\|_E$	$\|\| u_{ideal} - u_h \|\|_{L\infty}$
$\pi/12$	5,718	0.672812258	0.127176549	0.764582936
$\pi/10$	6,864	0.071726134	0.019009030	0.078285617
$\pi/8$	8,580	0.070499532	0.003193354	0.008051766
$\pi/6$	11,440	0.056004520	0.000542701	0.000833950
$\pi/3$	22,880	0	0	0

Table 6
A posteriori errors occur with the finite triangular space-discretization over a corresponding Venus-problem domain that is analyzed with our solution approximations in the assorted norm manifolds for each maximum lowest angle.

Angle	# of Elements	$\|\| u_{ideal} - u_h \|\|_L^2$	$\|\| u_{ideal} - u_h \|\|_E$	$\|\| u_{ideal} - u_h \|\|_{L\infty}$
$\pi/12$	35,622	0.104688985	0.198669791	0.947548082
$\pi/10$	42,747	0.011149470	0.029598089	0.096578262
$\pi/8$	53,433	0.010959054	0.004963191	0.009880965
$\pi/6$	71,246	0.008707205	0.000843668	0.001016868
$\pi/3$	142,492	0	0	0

adaptation for a greater extent of solid customization. Our highly refined models have been equipped to achieve adaptation refinements over 3D grid areas. Our exclusive design methods with self-adaptations were taken into account both manually and virtually in an automated design for improved performance. Multidimensional restorations with automated conditioning of mixed boundary conditions for autorefinement have been readjusted in our overall system. Throughout the fully automated refinements, the solid-state models have been transformed into well-remodeled procedural enrichments through our unique method.

Declarations

Author contribution statement

Aykut Zongur: Conceived and designed the experiments; Performed the experiments; Analyzed and interpreted the data; Contributed reagents, materials, analysis tools or data; Wrote the paper.

Funding statement

This research did not receive any specific grant from funding agencies in the public, commercial, or not-for-profit sectors.

Competing interest statement

The authors declare no conflict of interest.

Additional information

No additional information is available for this paper.

References

[1] J. Boissonnat, Geometric structures for three dimensional shape representation, ACM Trans. (1984) 266–286.
[2] M. Kilian, H. Pottmann, Geometric modeling in shape space, ACM Trans. 26 (3) (2007) 64.
[3] M. Pauly, M. Gross, Shape modeling with point-sampled geometry, ACM Trans. 22 (3) (2003) 641–650.
[4] F. Bornemann, P. Deuflhard, The cascading multigrid method for elliptic problems, Numer. Math. 75 (2) (1996) 135–152.
[5] F. Bernardini, D. Schikore, Automatic reconstruction of 3D CAD models from digital scans, Int. J. Comput. Geom. Appl. 9 (5) (1999) 327–370.
[6] A. Lee, W. Sweldens, MAPS: multiresolution adaptive parameterization of surfaces, ACM Trans. (1998) 95–104.
[7] D. Nehab, R. Ramamoorthi, Efficiently combining positions and normals for precise 3D geometry, ACM Trans. 24 (3) (2005) 536–543.
[8] H. Okamoto, M. Wunsch, A Geometric Construction of Continuous, Strictly Increasing Singular Functions, vol. 83, Japan Academic Seria-A, 2007, pp. 114–118, euclid.jpa.1200672011.
[9] E. Mücke, H. Edelsbrunner, Three-dimensional alpha shapes, ACM Trans. 13 (1) (1994) 43–72.
[10] A. Okabe, K. Sugihara, Spatial Tessellations: Concepts and Applications of Voronoi Diagrams, Wiley, 1992.
[11] Q. Du, M. Gunzburger, Centroidal Voronoi tesselations: applications and algorithms, SIAM Rev. 41 (4) (1999) 637–676.
[12] Y. Ohtake, H. Seidel, 3D scattered data approximation with adaptive compactly supported radial basis functions, SMI (2004) 31–39.
[13] Fast Fourier Transform, FFT, 2017. Access Link, http://www.fftw.org.
[14] A. Chorin, Numerical solution of the Navier-Stokes equations, Math. Comput. (22) (1968) 745–762.
[15] I. Daubechies, 10 Lectures on Wavelets, Society for Industrial and Applied Mathematics, Philadelphia, 1992.
[16] V. Girault, P.A. Raviart, Finite Element Methods for Navier-Stokes Equations: Theory and Algorithms, Springer-Verlag, 1986.
[17] O. Schall, H.P. Seidel, Error-guided adaptive Fourier-based surface reconstruction, Comput. Aided Des. 39 (5) (2007) 421–426.
[18] H. Edelsbrunner, Geometry and Topology for Mesh Generation, Cambridge University Press, 2006.